Received: 15 December 2021 | Revised: 9 April 2022 | Accepted: 2 May 2022

IET Science, Measurement & Technology

DOI: 10.1049/smt2.12108

The Institution of Engineering and Technology WILEY

ORIGINAL RESEARCH

# A free-cutting mesh strategy for optimal shape synthesis in magnetics

F. Dassi[1] | P. Di Barba[2] | A. Russo[1,3]

[1]Dipartimento di Matematica e Applicazioni, Università di Milano–Bicocca, Via Cozzi 55, Milano, Italy

[2]Dipartimento di Ingegneria Industriale e dell'Informazione, Università di Pavia, Via Adolfo Ferrata 5, Pavia, Italy

[3]IMATI-CNR, Via Ferrata 5/A, Pavia, Italy

**Correspondence**
F. Dassi, Dipartimento di Matematica e Applicazioni, Università di Milano–Bicocca, Via Cozzi 55, I-20153, Milano, Italy.
Email: franco.dassi@unimib.it

Funding information
None

**Abstract**

The authors propose an innovative technique for dealing with optimal shape design problems that exploits the flexibility of the virtual element method in generating meshes composed of general polygonal and polyhedral elements. Virtual element method and finite element method can coexist on the same discretized domain; therefore, the possibility of dealing with hanging nodes and gluing sub-domain meshes is ensured. Accordingly, the shape synthesis of a magnetic pole is considered as the case study. It is shown that the proposed technique is effective in handling the shape variations dictated by an algorithm of evolutionary optimisation.

## 1 | INTRODUCTION

The virtual element method (VEM) is a recent and successful method for the numerical solution of partial differential equations [1]. VEM can be considered as an evolution of the finite element method (FEM) that can make use of very general decompositions of the computational domain into polygonal or polyhedral elements. Moreover, VEM allows for a generic degree of accuracy, that corresponds to the polynomial degree in standard FEM, and exhibits an excellent robustness with respect to mesh distortions. As a consequence of this flexibility, VEM may be particularly useful, for example, in the presence of solutions with varying regularity, for grid adaptation, moving meshes, and in discretizing complex geometries. VEM and FEM share the same degrees of freedom on edges, hence they can coexist on the same mesh. In the case of triangular elements, it is advisable to use FEM because, apart from the linear case, VEM on triangles has more internal degrees of freedom with respect to FEM. Furthermore, general polygons do not have a reference element, so the computation of local stiffness matrices is more expensive with respect to FEM. Hence, it is recommended to use virtual elements only in those parts of the domain where they are really needed.

In the framework of magnetostatic problems, the VEM was developed both for the potential and the Kikuchi formulations in a linear and non-linear case, see, for instance, [2, 3]. Furthermore, such kind of problems attracted other polytopal technologies such as hybrid high order (HHO) and discontinuous Galerkin (DG) methods, see, for instance, [4–8].

We focus on the VEM and we exploit such a method in an optimal shape design problem. We consider the benchmark problem [9, 10] that is one of the classical optimal shape design problem of a magnetic pole for synthesising a uniform field profile in a region of interest. We take a fixed background mesh composed of equal squares, and at each step of the iteration we 'cut' the squares following the computed shape of the magnetic pole. The cuts of the squares generate polygons which are treated as VEM. The idea of cutting elements is not new, see, for instance, [11]. Our approach is different, since VEM can deal with general polygonal and polyhedral elements and does not require ad hoc constructions depending on the shape of the cut.

## 2 | MAGNET SHAPE DESIGN OPTIMISATION: AN OVERVIEW

Shaping a magnetic pole for synthesising a field is a typical problem in computational electromagnetism and can be considered as a benchmark against which testing various methods. In general, a set of points describing the iron/air boundary are to be varied in position in order that the magnetic field over a prescribed region of space tends to a given distribution. Typical distribution are a uniform field in a dipole, uniform field gradient for a quadrupole or some other criterion like, for instance, the field circulation or the field flux to be equal to a given value. A uniform field within a region of interest is usually a basic requirement for many applications, like it happens, for example, in the area of nuclear magnetic resonance or clinical hyperthermia based on magnetic fluids. Pioneering contributions to optimal shape design methods can be found, for example, in [9, 12] where the optimal shape design of an iron-cored electromagnet is developed, while the synthesis of a distributed field winding is considered in [13].

To achieve the goal of field syntheses, the optimal shape design model can be reformulated as an inverse problem which is subsequently solved by means of an iterative technique of numerical optimisation. A suitable functional is the infinity norm of the discrepancy between actual and prescribed flux density in the region of interest: The unknown is the pole shape, belonging to the class of uniformly Lipschitzian open sets in $\mathbb{R}^2$ or $\mathbb{R}^3$, which minimises the functional. There are many strategies related to such issue. In [14, 15] a parametric optimisation strategy was used to design a coreless winding as the field source. In [10] a non-parametric approach was proposed in order to optimise the shape of a ferrite core. In all these cases, given a feasible shape, that is, a shape fulfilling the problem constraints, the relevant field-analysis problem has to be solved via a finite element (FE) model in two or three dimensions.

Whatever the optimisation strategy, during the optimisation procedure, the mesh discretising the magnetic pole is modified so the problem of handling a deformed mesh arises. Based on the traditional approach, at each iteration new triangles are generated. Indeed, if the area of a triangle becomes too large, any triangle can be split into three new triangles using its centre as a new node [16].

Alternatively, the triangle can be split into four new triangles using the edge midpoints as new nodes, and then the neighbouring triangles are accordingly sub-divided into two new elements. In doing this, a limitation on the angle width is introduced in order to avoid the creation of too sharp triangles. In particular, in [10] two strategies for updating the profile of the pole shape were implemented: In the fixed-grid strategy the region to synthesise is subdivided into several square sub-regions, whose material property can be attributed to either air or ferrite. This way, the unknown profile is approximated by means of a staircase-shaped line, and a structured mesh discretises the synthesis region: The material permeability (either ferrite or air) is updated, and the field analysis is repeated. This way, the FE mesh does not change, while the distribution of magnetic permeability changes (fixed topology, variable material). Alternatively, in the variable-grid strategy, the unknown profile is approximated by means of a polygonal line defined by a number of moving nodes, and the FE mesh is accordingly regenerated.

In contrast, the VEM approach to field analysis suggests a completely new way of handling the shape variation during the optimisation procedure: The key idea is to start from a uniform mesh composed, for example, of quadrilateral elements regularly spaced, and then to introduce suitable cuts by means of lines which join vertices or edges of the quadrilateral mesh. This way, the cutting line splits the original quadrilateral element into a pair of polygonal elements which are naturally handled in the VEM model; in the case of the magnet design, the cutting line represents the air–ferrite boundary defining the magnet shape dictated by the optimisation algorithm at the current iteration.

We consider the optimal design of a large-size electromagnet for applications in magneto-fluid hyperthermia (MFH). Indeed, MFH represents an important application of magnets in medical therapy; however, the particular case study does not limit the general validity of the proposed method by any means. Actually, magnetic fluids have a good potential for clinical hyperthermia due to their capability of concentrating power. The heat generated by magnetic nanoparticles suspended in a fluid depends on the squared value of an applied time-harmonic field so nanoparticles excited by an AC field can be exploited to treat tumoral issues [17–20]. Indeed, experiments with MFH have shown that human tumour cells are homogeneously inactivated after AC magnetic field excitation of magnetic fluids injected in the tumour region [21]. Since the power density generated by nanoparticles is a function of the applied magnetic field [20–22], field uniformity and field strength are a twofold prerequisite for homogeneously heating the tumour tissue at a therapeutic temperature, without damaging the neighbouring healthy tissues.

A typical device for clinical MFH is characterised by a magnetic core made of ferrite and exhibiting three limbs. Two series-connected current-carrying coils are wound on the central limb which exhibits a wide air gap, where the patient is accommodated during the treatment; the system has proven its capability and practicability for heat treatment in deep regions of the human body [21]. So, the design challenge is to shape the magnetic pole in such a way that a uniform field of prescribed strength takes place in the region of interest.

## 3 | THE DEVICE MODEL

A quarter of the model geometry here considered is shown in Figure 1: A ferrite core fills in region $\Omega_F$, while an air gap 30 cm high and 20 cm long incorporates the region of interest $\Omega_I$, that is, an air region where the degree of uniformity of flux density is controlled. A non-linear material is considered in the model. More specifically, we consider the non-linear relation between $\mathbf{H}$ and $\mu_r$ of iron silicon with width of 0.5 mm [23]. The complementary domain includes the winding cross-section $\Omega_J$, which is composed of 16 turns and carries a sinusoidal current of 150 A rms at 100 kHz, and an air region, $\Omega_A$.

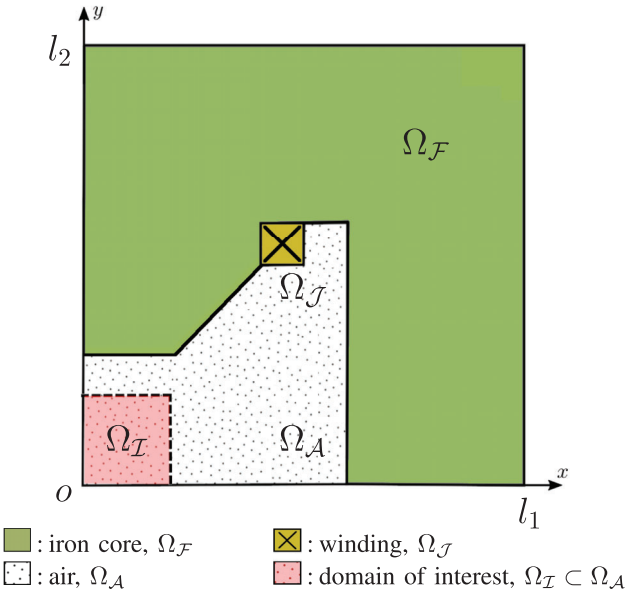


**FIGURE 1** Domain to consider

Although in MFH applications the magnet is excited by a sinusoidal current and, as a consequence, a time-harmonic field takes place, here we consider a static case, that is, the current is constant in time and generates a static field. This choice does not imply a loss of generality since we aim at shaping just the field pattern and we are not interested in the simulation of induced current in the magnetic core. Moreover, any material exhibits a magnetic property in terms of tissue permeability which, at least in principle, could have an influence on the field pattern, and human body is no exception. This is the so-called *load effect*, that is, the reaction of organic material to an external magnetic field, the one driven by the electromagnet. It is worth noting that this load effect is patient dependent. Indeed, the permeability of tissues depends on some factors like, for instance, temperature. Furthermore, the field pattern is also influenced by shape and volume of the body which are again patient-dependent factors. Therefore, for the sake of generality, in the model we assumed to neglect the presence of human body.

## 4 | POTENTIAL FORMULATION

We consider the classical potential formulation in a two-dimensional domain $\Omega$, which consists of searching for the scalar field $\mathcal{A}$, that is, the potential associated with the magnetic induction field $\mathbf{B} = \mathbf{curl}\,\mathcal{A}$, such that

$$\operatorname{curl}(\mu^{-1}\,\mathbf{curl}\,\mathcal{A}) = j \quad \text{in } \Omega, \tag{1}$$

plus boundary conditions on $\partial\Omega$. The two-dimensional **curl** and the scalar curl are defined as

$$\mathbf{curl}\,\mathcal{A} := (\partial_2\mathcal{A}, -\partial_1\mathcal{A}) \quad \text{and} \quad \operatorname{curl}\mathbf{A} := \partial_1 A_2 - \partial_2 A_1\,, \tag{2}$$

respectively. In Equation (1), the scalar $\mu$ represents the material permeability, while $j$ is the assigned current density which in two dimensions is a scalar quantity. It turns out to be

$$\begin{aligned}\operatorname{curl}(\mu^{-1}\,\mathbf{curl}\,\mathcal{A}) &= \partial_1(-\mu^{-1}\partial_1\mathcal{A}) - \partial_2(\mu^{-1}\partial_2\mathcal{A}) \\ &= -\operatorname{div}(\mu^{-1}\nabla\mathcal{A})\,,\end{aligned}$$

so Equation (1) becomes

$$-\operatorname{div}(\mu^{-1}\nabla\mathcal{A}) = j \quad \text{in } \Omega\,,$$

subject to appropriate boundary conditions. For our problem we take homogeneous Dirichlet boundary conditions along $x = 0$, $x = l_1$, and $y = l_2$, while homogeneous Neumann boundary conditions along $y = 0$, see Figure 1.

## 5 | THE VEM FOR THE POISSON PROBLEM

As we have seen, the potential formulation for magnetostatics consists of a single Poisson's equation with variable diffusion. In this section, we will describe the VEM in the simpler case of Poisson's equation with constant diffusion [1]. The same numerical method can be easily extended to a piecewise constant diffusion, while for the extension to the general case and the complete convergence analysis we refer to [24]. Moreover, it has been shown in [25] that the VEM can also be extended to the approximation of field oriented formulations.

Solving Poisson equation with constant diffusion and homogeneous Dirichlet boundary condition amounts to find the solution of the problem:

$$\begin{cases} -\Delta u = f & \text{in } \Omega \\ u = 0 & \text{on } \partial\Omega \end{cases} \tag{3}$$

which can be written in variational form as follows:

$$\begin{cases} \text{find } u \in H_0^1(\Omega) \text{ such that} \\ \displaystyle\int_\Omega \nabla u \cdot \nabla v\,\mathrm{d}\mathbf{x} = \int_\Omega f v\,\mathrm{d}\mathbf{x} \quad \text{for all } v \in H_0^1(\Omega). \end{cases} \tag{4}$$

Classical conforming FEMs require the following steps:

1) discretize the domain $\Omega$ with non-overlapping triangles $\{T\}$;
2) construct in each triangle through suitable basis functions a local space $V_h^k(T)$ made of polynomials up to degree $k$;
3) assemble the global space $V_h^k(\Omega) \subset H_0^1(\Omega)$ by gluing together in a continuous fashion the local spaces, respecting global boundary conditions;
4) solve the approximate variational problem

$$\begin{cases} \text{find } u_h \in V_h^k(\Omega) \text{ such that} \\ \displaystyle\int_\Omega \nabla u_h \cdot \nabla v_h\,\mathrm{d}\mathbf{x} = \int_\Omega f v_h\,\mathrm{d}\mathbf{x} \quad \text{for all } v_h \in V_h^k(\Omega). \end{cases} \tag{5}$$

If $k$ is an integer and $\mathcal{O} \subseteq \mathbb{R}^2$, we define $\mathbb{P}_k(\mathcal{O})$ as the space of polynomials of degree up to $k$ defined on $\mathcal{O}$. In the following, $\mathcal{O}$ will be a segment or a polygon.

We start with $k = 1$.

## 5.1 | The Courant triangle

Given a triangle $T$, we define the local FE space of degree 1 on $T$ by

$$V_h^1(T) := \mathbb{P}_1(T), \tag{6}$$

and if $V_1$, $V_2$, and $V_3$ are the vertices of $T$, the *local degrees of freedom* of a function $v_h \in V_h^1(T)$ are defined by

$$\mathrm{dof}_i(v_h) := v_h(V_i). \tag{7}$$

In other words, we are saying that a function $v_h \in V_h^1(T)$ is completely determined by its values at the vertices of the triangle.

The local basis functions $\varphi_i \in V_h^1(T)$ are defined in terms of the local degrees of freedom by the following condition:

$$\mathrm{dof}_i(\varphi_j) = \delta_{ij}. \tag{8}$$

The previous equation simply means that $\varphi_i$ is the only linear function that is one on vertex $V_i$ and zero on the other two vertices. The set of functions $\{\varphi_1, \varphi_2, \varphi_3\}$ is a basis for the space $V_h^1(T)$.

We now characterise the space $V_h^1(T)$ in a different way that will be crucial for the rest of the section. Given that there exists a unique harmonic function with assigned value at the boundary, the local space $V_h^1(T)$ can also be identified by the following properties:

- for each edge $e$ of $T$, $v_{h|e}$ is linear on $e$;
- the linear functions $v_{h|e}$ on the edges match at the common vertices;
- $v_h$ is harmonic inside, that is, $\Delta v_h = 0$ in $T$.

We underline that such properties will allow us to extend the definition of 'linear triangular element' to a general polygon.

## 5.2 | Extension to general polygons

The advantage of the previous characterisation is that it can be extended in a seamless way to a general polygon $P$ (even non-convex). In this case, we will obtain a space $V_h^1(P)$ that contains linear polynomials, together with other functions.

Given a polygon $P$, we define the space $V_h^1(P)$ in the following way:

- functions are linear on each edge and match at the vertices, see Figure 2;

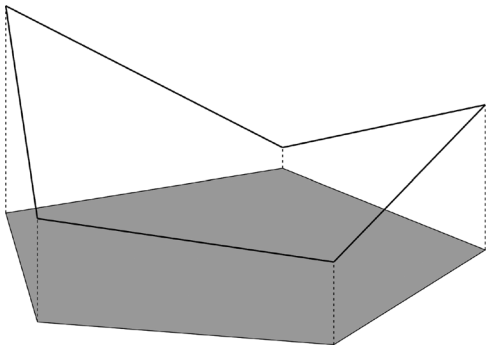

**FIGURE 2** Virtual functions are linear on each edge and match at the vertices

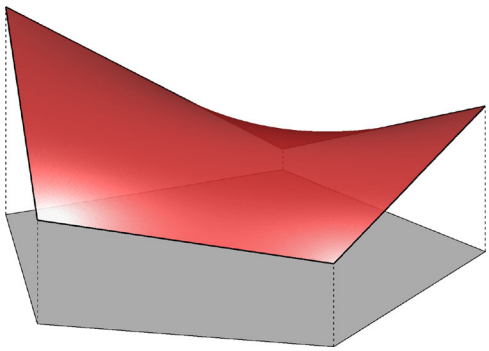

**FIGURE 3** Virtual functions are harmonic inside

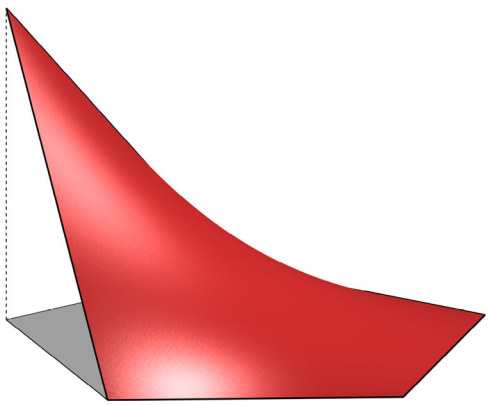

**FIGURE 4** Local basis function

- they are harmonic inside, see Figure 3.

It is clear that if $P$ is a triangle, we recover the Courant element.

The space $V_h^1(P)$ is known in literature as *harmonic FEs on a polygon*. The $i$-th local degree of freedom is still defined as the value of the function at vertex $i$; in fact, a function in $V_h^1(P)$ is completely determined by its values at the vertices. Hence

$$\text{dimension of } V_h^1(P) = \#\text{ of vertices of } P := N^V.$$

The local basis function $\varphi_i$ takes the value one at vertex $i$ and is zero at the other vertices, see Figure 4.

The key property of the space $V_h^1(P)$ is that it *contains linear polynomials*:

$$\mathbb{P}_1(P) \subseteq V_h^1(P). \tag{9}$$

In fact, if $p_1 \in \mathbb{P}_1(P)$ then

- ✓ $p_1$ is linear on each edge;
- ✓ $p_1$ is continuous on the boundary of the polygon;
- ✓ $p_1$ is harmonic: $\Delta p_1 \equiv 0$.

It has been proved in [1] that the fact that linear polynomials are inside the space ensures the same good approximation properties of classical FEM. If we were able to compute exactly the stiffness matrices, the method would converge at the expected rates. However, the value of $\varphi_i$ at a point inside the polygon is not readily available, since we only know that $\varphi_i$ is harmonic; hence the stiffness matrix cannot be simply computed by quadrature. This issue is addressed in Section 5.4.

## 5.3 | The global space

The global FE space is defined in the same way as for classical FE: The local spaces on adjacent polygons sharing an edge glue together continuously through the common edge, producing globally continuous approximation functions.

We point out that the extra non-linear functions of $V_h^1(P)$, which exist if the polygon is not a triangle, ensure continuity of potential when two elements are joined together, giving a conformal method. If we allow discontinuous functions across elements, we could define the local space on each polygon simply as $\mathbb{P}_1(P)$. This choice leads to the DG method. The main difference with respect to VEM is that DG is non-conformal.

## 5.4 | The projection $\Pi_1^\nabla$

We cannot compute in a cheap way the value of a function $v_h \in V_h^1(P)$ inside $P$ starting from the degrees of freedom. In fact, we can easily recover the function on the boundary, being linear on each edge; but computing the value inside the polygon would require the solution of Laplace equation with given boundary data. Hence it is not feasible to directly compute the local stiffness matrices by quadrature.

We show that we can compute directly from the degrees of freedom a linear polynomial $p_1$ that approximate $v_h$ in the following integral sense:

$$\int_P \nabla(p_1 - v_h) \cdot \nabla q_1 \, d\mathbf{x} = 0 \quad \text{for all linear polynomials } q_1. \tag{10}$$

In other words, $p_1$ is the projection of $v_h$ with respect to the scalar product $\int_P \nabla u \cdot \nabla v \, d\mathbf{x}$. We denote the projection $p_1$ by $\Pi_1^\nabla v_h$. Note that the null space of the operator $\Pi_1^\nabla$, that is, the subspace of $V_h^1(P)$ such that $\Pi_1^\nabla v_h = 0$, has dimension $N^V - 3$ since $\dim \mathbb{P}_1(P) = 3$.

In order to show that (10) can be solved by knowing only the degrees of freedom of $v_h$ (i.e. the value of $v_h$ at the vertices of the polygon), we argue in the following way.

If we express the unknown $\Pi_1^\nabla v_h$ in the monomial basis of linear polynomials, namely $\{1, x, y\}$, and we let $q_1$ vary among $\{1, x, y\}$, we obtain a $3 \times 3$ linear system. Let $m_1 := 1$, $m_2 := x$, and $m_3 := y$; we write

$$\Pi_1^\nabla v_h = \sum_{\alpha=1}^{3} c_\alpha m_\alpha, \quad c_\alpha = \text{unknowns}$$

and (10) becomes

$$\int_P \nabla\left(\sum_{\alpha=1}^{3} c_\alpha \, m_\alpha - v_h\right) \cdot \nabla m_\beta \, d\mathbf{x} = 0, \quad \beta = 1, 2, 3$$

or equivalently

$$\sum_{i=1}^{3} c_\alpha \left[\int_P \nabla m_\alpha \cdot \nabla m_\beta \, d\mathbf{x}\right] = \int_P \nabla v_h \cdot \nabla m_\beta \, d\mathbf{x}, \ \beta = 1, 2, 3. \tag{11}$$

The $3 \times 3$ matrix $\int_P \nabla m_\alpha \cdot \nabla m_\beta \, d\mathbf{x}$ is singular, since it has the first row (and the first column) identically zero: in fact $\nabla m_1 \equiv 0$. This feature reflects the fact that (10) determines the projection $\Pi_1^\nabla v_h$ only up to a constant, or, in other words, that (10) determines only the gradient of $\Pi_1^\nabla v_h$. In order to completely recover $\Pi_1^\nabla v_h$ we need to substitute the first equation in (11) with a (computable) condition guaranteeing that when $v_h$ is constant, $\Pi_1^\nabla v_h = v_h$. This can be achieved by asking, for instance, that

$$\sum_{i=1}^{N^V} \Pi_1^\nabla v_h(V_i) = \sum_{i=1}^{N^V} v_h(V_i).$$

The final $3 \times 3$ final linear system is then

$$\begin{cases} \displaystyle\sum_{\alpha=1}^{3} c_\alpha \sum_{i=1}^{N^V} m_\alpha(V_i) = \sum_{i=1}^{N^V} v_h(V_i) \quad \text{(first row)} \\ \displaystyle\sum_{\alpha=1}^{3} c_\alpha \left[\int_P \nabla m_\alpha \cdot \nabla m_\beta \, d\mathbf{x}\right] = \int_P \nabla v_h \cdot \nabla m_\beta \, d\mathbf{x}, \ \beta = 2, 3. \end{cases} \tag{12}$$

We need to show that the matrix and the right-hand side of the linear system (12) are directly computable from the degrees of freedom of $v_h$, that is, the values of $v_h$ at the vertices.

- The matrix of (12) clearly does not depend on $v_h$, and its coefficients are simple computable from the monomial basis which is explicitly given;

- as far as the right-hand side is concerned, in the first line of (12) there are the values of $v_h$ at the vertices, while in lines 2 and 3 there is the expression

$$\int_P \nabla v_h \cdot \nabla m_\beta \, \mathrm{d}\mathbf{x}, \quad \beta = 2, 3.$$

Integrating by parts, we have

$$\int_P \nabla v_h \cdot \nabla m_\beta \, \mathrm{d}\mathbf{x} = -\int_P v_h \Delta m_\beta \, \mathrm{d}\mathbf{x} + \int_{\partial P} v_h \frac{\partial m_\beta}{\partial n} \, \mathrm{d}s = \int_{\partial P} v_h \frac{\partial m_\beta}{\partial n} \, \mathrm{d}s$$

since $\Delta m_\beta \equiv 0$, $m_\beta$ being a linear monomial or a constant. Recalling that $v_h$ is linear on each edge, from the degrees of freedom of $v_h$, that is, the values of $v_h$ at the vertices, we can easily reconstruct $v_h$ on the boundary of $P$ and hence compute the boundary term.

## 5.5 | The local stiffness matrix for the Poisson equation

Given that the degrees of freedom of the basis functions $\varphi_i$ are known by definition (they are all zeros except the $i$-th which is 1), we can easily compute $\Pi_1^\nabla \varphi_i$ and it seems to be a good idea to make the following approximation of the 'true' local stiffness matrix for the Poisson equation:

$$\int_P \nabla \varphi_j \cdot \nabla \varphi_i \, \mathrm{d}\mathbf{x} \approx \int_P \nabla \Pi_1^\nabla \varphi_j \cdot \nabla \Pi_1^\nabla \varphi_i \, \mathrm{d}\mathbf{x}. \tag{13}$$

However, this is not appropriate because the $N^V \times N^V$ matrix $\int_P \nabla \Pi_1^\nabla \varphi_j \cdot \nabla \Pi_1^\nabla \varphi_i \, \mathrm{d}\mathbf{x}$ is rank-deficient, giving rise to a singular global matrix. The 'right' rank for the local matrix $\int_P \nabla \Pi_1^\nabla \varphi_j \cdot \nabla \Pi_1^\nabla \varphi_i \, \mathrm{d}\mathbf{x}$ would be $N^V - 1$, because the constant functions are clearly in the kernel but they are ruled out by the global boundary conditions, giving at the end an invertible matrix. Instead, it can be easily shown that the rank is 2 which is strictly less than $N^V - 1$ unless $P$ is a triangle. For, we have already observed that the null space of the projection operator $\Pi_1^\nabla$ has dimension $N^V - 3$, and the gradient annihilates the constant functions. In the global space the constant functions are ruled out by the boundary condition, but the global stiffness matrix (in general) remains singular, unless all polygons are triangles.

## 5.6 | Consistency

Using (13) amounts to replace (5) with

$$\begin{cases} \text{find } u_h \in V_h^1(\Omega) \text{ such that} \\ \displaystyle\int_\Omega \nabla \Pi_1^\nabla u_h \cdot \nabla \Pi_1^\nabla v_h \, \mathrm{d}\mathbf{x} = \int_\Omega f v_h \, \mathrm{d}\mathbf{x} \quad \text{for all } v_h \in V_h^1(\Omega), \end{cases} \tag{14}$$

where

$$\int_\Omega \nabla \Pi_1^\nabla u_h \cdot \nabla \Pi_1^\nabla v_h \, \mathrm{d}\mathbf{x} = \sum_T \int_T \nabla \Pi_1^\nabla u_h \cdot \Pi_1^\nabla \nabla v_h \, \mathrm{d}\mathbf{x}.$$

We do not discuss how to approximate the load term; we refer to [26] for the details.

As explained before, problem (14) is singular, hence in general it has no solution. However, it is *consistent* in the following sense: If the exact solution $u$ is a global linear polynomial $p_1$, then it is a solution of (14) as well. In fact, by (4), $u = p_1$ would solve

$$\int_\Omega \nabla p_1 \cdot \nabla v_h \, \mathrm{d}\mathbf{x} = \int_\Omega f v_h \, \mathrm{d}\mathbf{x} \quad \text{for all } v_h \in V_h^1(\Omega).$$

By the definition of the projector $\Pi_1^\nabla$, we have

$$\int_\Omega \nabla p_1 \cdot \nabla v_h \, \mathrm{d}\mathbf{x} = \int_\Omega \nabla p_1 \cdot \nabla \Pi_1^\nabla v_h \, \mathrm{d}\mathbf{x} \tag{15}$$

and since $\Pi_1^\nabla p_1 = p_1$, we also have

$$\int_\Omega \nabla p_1 \cdot \nabla \Pi_1^\nabla v_h \, \mathrm{d}\mathbf{x} = \int_\Omega \nabla \Pi_1^\nabla p_1 \cdot \nabla \Pi_1^\nabla v_h \, \mathrm{d}\mathbf{x}.$$

Hence $p_1$ satisfies Equation (14):

$$\int_\Omega \nabla \Pi_1^\nabla p_1 \cdot \nabla \Pi_1^\nabla v_h \, \mathrm{d}\mathbf{x} = \int_\Omega f v_h \, \mathrm{d}\mathbf{x} \quad \text{for all } v_h \in V_h^1(\Omega).$$

Property (15) is crucial: It ensures *consistency*. However, (15) alone it is not enough: We need to add *stability*.

## 5.7 | Stabilisation

We need to supplement (14) with a *stabilisation term* that

- guarantees existence and uniqueness;
- does not spoil consistency (Equation (15));
- is defined element by element.

It turns out that we can add to (14) a term of the form

$$S\big((\mathrm{I} - \Pi_1^\nabla)u_h, (\mathrm{I} - \Pi_1^\nabla)v_h\big) = \sum_T S_T\big((\mathrm{I} - \Pi_1^\nabla)u_h, (\mathrm{I} - \Pi_1^\nabla)v_h\big), \tag{16}$$

where $S_T(\cdot, \cdot)$ is a symmetric coercive bilinear form that scales in the right way. Note that if one of the entries is a linear polynomial $p_1$, since $(\mathrm{I} - \Pi_1^\nabla)p_1 \equiv 0$ the term (16) is zero, so consistency is preserved.

It can be shown that under certain assumption on the mesh, we have convergence at the expected rates. There is much freedom in the choice of the local stability bilinear form $S_T(\cdot,\cdot)$. One possibility in this simple case is to define $S_T(\cdot,\cdot)$ by $S_T(\varphi_i,\varphi_j)=\delta_{ij}$.

### 5.8 | The case $k=2$

We briefly consider the case $k=2$. As for FE on triangles, we need to add the middle point of each edge in order to have polynomial of degree 2 on each edge. Since the Laplacian of a degree 2 polynomial is constant, we substitute the condition $\Delta v_h \equiv 0$ with $\Delta v_h = \text{constant}$. The degrees of freedom of a function $v_h \in V_h^2(P)$ are:

- boundary degrees of freedom: as for FEM, the pointwise values at the vertices and at the middle point of the egdes;
- internal degrees of freedom: the mean value on $P$, that is, $\frac{1}{|P|}\int_P v_h \,\mathrm{d}\mathbf{x}$.

Hence we have $\dim V_h^2(P) = 2N^V + 1$ and it is immediate to verify that $\mathbb{P}_2(P) \subseteq V_h^2(P)$. Note that in this case if $P$ is a triangle we do not recover the classical FEs of order 2 but a larger space.

We need to check that we can compute the $\Pi_2^\nabla$ projection starting from the degrees of freedom. Considering the construction above for the case $k=1$, it turns out that we only need to be able to compute the right-hand side of the linear system, that is,

$$\int_P \nabla v_h \cdot \nabla m_\beta \,\mathrm{d}\mathbf{x}, \quad \beta = 1,2,\dots,6,$$

where $m_\beta$ is a monomial in two variables up to degree 2 ($m_1 := 1$, $m_2 := x$, $m_3 := y$, $m_4 := x^2$, $m_5 := xy$, $m_6 := y^2$). Integrating by parts, we have as before

$$\int_P \nabla v_h \cdot \nabla m_\beta \,\mathrm{d}\mathbf{x} = -\int_P v_h \Delta m_\beta \,\mathrm{d}\mathbf{x} + \int_{\partial P} v_h \frac{\partial m_\beta}{\partial n}\,\mathrm{d}s. \quad (17)$$

This time $\Delta m_\beta$ is zero for $\beta = 1,2,3$ but is constant for $\beta = 4,5,6$. Hence

$$\int_P v_h \Delta m_\beta \,\mathrm{d}\mathbf{x}$$

can be readily computed starting from the internal degree of freedom. The rest of the construction works in the same way.

### 5.9 | The general case

In the general case, the functions $v_h \in V_h^k(P)$ are polynomials of degree $k$ on each edge of $P$, they match at the vertices and

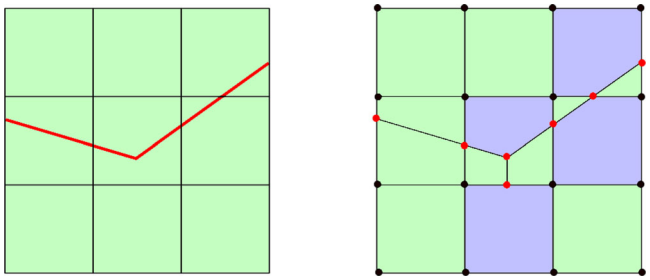

**FIGURE 5** Example of cutting squares where we highlight the elements where we use FEM, light green, and the ones where we exploit VEM, light blue. Note that a VEM element can be fully surrounded by FEM elements

$\Delta v_h$ is a polynomial of degree $k-2$. These conditions ensure that $\mathbb{P}_k(P) \subseteq V_h^k(P)$. The boundary degrees of freedom are the pointwise values at the vertices and at $k-1$ internal nodes on each edge (which can be taken equispaced as in classical FEM), and the internal degrees of freedom are the *moments* up to order $k-2$ in $P$, that is,

$$\frac{1}{|P|}\int_P v_h m \,\mathrm{d}\mathbf{x}, \quad m \text{ monomial up to degree } k-2. \quad (18)$$

If we consider Equation (17) in this case, we observe that $\Delta m_\beta$ is a polynomial of degree up to $k-2$, so the term $\int_P v_h \Delta m_\beta \,\mathrm{d}\mathbf{x}$ can be computed directly from the internal degrees of freedom of $v_h$. We refer to [26] for a detailed description.

## 6 | VEM AND FEM: A FREE-CUTTING STRATEGY

In practice, we can mix VEM and FEM in a seamless way because the degrees of freedom on the edges are the same. There are several ways to take advantage of this fact.

In view of a mesh strategy that naturally complies with the shape variations characterising a shape design process, the key idea is to start from a uniform mesh in the optimising region, composed, for example, of quadrilateral elements regularly spaced, and then introduce suitable cuts by segments whose end-points are located at the vertexes or on edges of the background mesh. Consequently the original quadrilateral element is cut in polygons that, if they are not triangles or quadrilaterals, are naturally handled by VEM and there is no need of sub-triangulating or re-building the mesh.

Actually, there are three situations to handle:

- *A segment cutting a square into two quadrilaterals*: in this case, the two quadrilaterals with be treated via FEM, see the first column of the mesh in Figure 5.
- *A vertex of the profile falling into the square*: in this case, we cut vertically the square to avoid non-convex elements and the square is divided into three polygons, see the second column of the mesh in Figure 5. The resulting polygons could be triangles, quadrilaterals, or pentagons. We notice that the square below will become a pentagon.

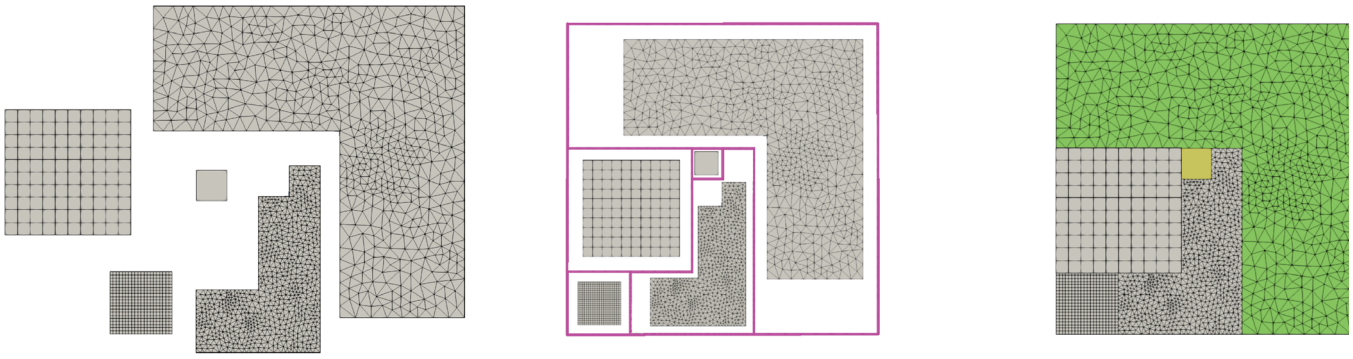

(a) Initial meshes. (b) Gluing guidelines. (c) The resulting mesh glued.

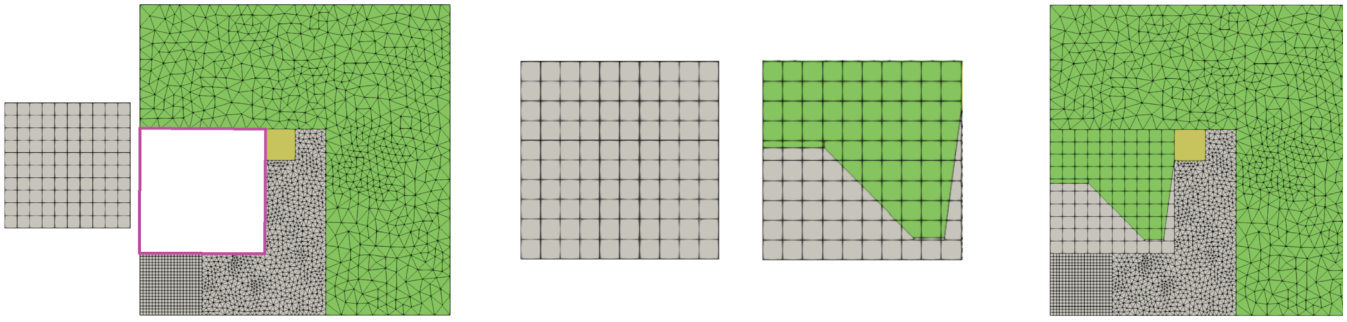

(d) Extraction of $\Omega_{\mathcal{O}}$. (e) Draw the computed magnet profile on $\Omega_{\mathcal{O}}$ and cut elements. (f) $\Omega_{\mathcal{O}}$ is glued back.

**FIGURE 6** The whole meshing procedure during optimisation

- *A segment cutting a square into a triangle and a pentagon*: the triangle will be treated via FEM, the pentagon via VEM, see the third column of the mesh in Figure 5.

The whole meshing process is summarised in Figure 6. Each piece of the domain is discretised at the beginning and then glued together, see Figure 6a–c. Such a procedure is possible and straightforward since hanging nodes are naturally handled by VEM. Then, the mesh associated with region $\mathbf{\Omega_{\mathcal{O}}}$ is extracted and the structured quadrilateral mesh is stored, see Figure 6d. Given the computed profile, that is, the locations of design variables, such a profile is drawn over this structured mesh, see Figure 6e, and glued back to the mesh *without* region $\mathbf{\Omega_{\mathcal{O}}}$, Figure 6f. In the optimisation process described in Section 7.3, the meshing part jumps from Figure 6f until the minimum is reached.

There are several strategies to re-meshing. One possible way is to resort to meshless methods, see, for example, [27–29]. In this case, connections among nodes are not required and it is based on the interaction of each node with all its neighbours. Another possible strategy is to use mortar methods, see, for instance, [30, 31]. Indeed, this method is also able to deal with hanging nodes and, consequently, it handles the mesh coming from such cutting and gluing process. However, we here prefer to fully preserve an FE approach since its methodological background is well assessed in the literature.

## 7 | THE OPTIMISATION STRATEGY

In this section, we proceed with the validation of the proposed optimisation algorithm. To better understand the whole procedure, we split this section in the following parts. In Section 7.1 we introduce two objective functions which will drive the optimisation. In Section 7.2 we define the design variables we are using for the proposed study. Then, in Section 7.3, we explain the results obtained via the proposed semi-random walk. Finally, in Section 7.4 we show several numerical experiments.

### 7.1 | Objective functions

The optimisation procedure aims at having a uniform upward-pointing magnetic field $\mathbf{B}_0 = (0, 20)$ mT inside the region of interest $\mathbf{\Omega}_{\mathcal{I}}$. Consider a magnet profile $\Gamma_{\mathcal{P}}$ and let $\mathbf{B}_{\Gamma_{\mathcal{P}}}$ be the magnetic field associated with the profile $\Gamma_{\mathcal{P}}$. If $\mathbf{B}_{\Gamma_{\mathcal{P}}}(\mathbf{x})$ equals $\mathbf{B}_0$ on $\Gamma_{\mathcal{I}}$, then $\mathbf{B}(\mathbf{x}) = \mathbf{B}_0$ on the whole $\mathbf{\Omega}_{\mathcal{I}}$. Indeed, we have homogeneous Neumann and Dirichlet boundary conditions on $y = 0$ and $x = 0$, respectively, and no current source inside $\mathbf{\Omega}_{\mathcal{I}}$,

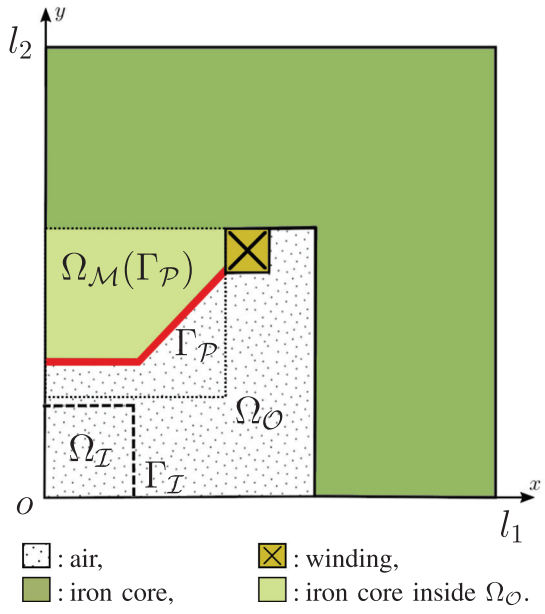


**FIGURE 7** We highlight the part of the domain involved in the optimisation procedure. The domain of interest $\Omega_{\mathcal{I}}$ and its boundary $\Gamma_{\mathcal{I}}$. The domain where the magnet profile, $\Gamma_{\mathcal{P}}$, varies $\Omega_{\mathcal{O}}$ and the varying iron core region, $\Omega_{\mathcal{M}}(\Gamma_{\mathcal{P}})$

that is, $j = 0$, so $A$ has linear variation with respect to $x$, it is constant in $y$ and therefore $\mathbf{curl}\,(A) = \mathbf{B}_0$.

As a consequence of this observation we look for the minimum of the following functional:

$$\psi_1(\Gamma_{\mathcal{P}}) := \max_{\mathbf{x}\in\Gamma_{\mathcal{I}}} \frac{\|\mathbf{B}_{\Gamma_{\mathcal{P}}}(\mathbf{x}) - \mathbf{B}_0\|}{\|\mathbf{B}_0\|}, \tag{19}$$

where $\|\cdot\|$ is the standard Euclidean norm. This quantity is a good measure of how much the resulting magnetic field is uniform inside the whole $\Omega_{\mathcal{I}}$. Moreover, since we have the normalising factor $\|\mathbf{B}_0\|$ and we are computing the difference between the actual field and the target one, the more $\psi_1(\Gamma_{\mathcal{P}})$ is close to zero, the more the resulting field $\mathbf{B}_{\Gamma_{\mathcal{P}}}$ is close to $\mathbf{B}_0$ inside $\Omega_{\mathcal{I}}$.

The function defined in Equation (19) does not contain any information about the geometry at hand. However, starting from the results in [9, 10], we know that a uniform magnetic field is achieved when we 'dig' the magnet. To advance this digging process, we propose the following correction of $\psi_1$:

$$\psi_2(\Gamma_{\mathcal{P}}) := \psi_1(\Gamma_{\mathcal{P}}) + \lambda \frac{|\Omega_{\mathcal{M}}(\Gamma_{\mathcal{P}})|}{|\Omega_{\mathcal{O}}|}, \tag{20}$$

where $\lambda \in [0, 1]$ is a penalty factor, $\Omega_{\mathcal{M}}(\Gamma_{\mathcal{P}})$ is the region occupied by the magnet inside the optimising region $\Omega_{\mathcal{O}}$, see Figure 7, and $|\cdot|$ denotes the area of a region. The correction made by this new term penalise configurations where the magnet inside the optimising region is more enlarged. Consequently, the functional $\psi_2$ will prefer configurations that are 'dug' as in [9, 10].

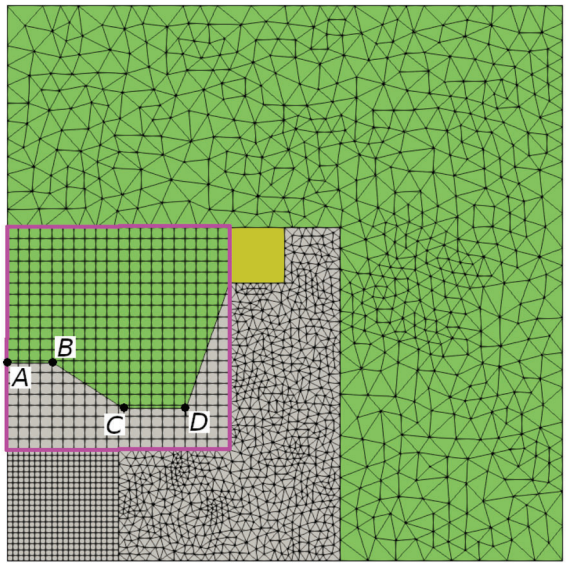


**FIGURE 8** Mesh of the computational domain where we take the `4pt` strategy. We also highlight the design points $A$, $B$, $C$, and $D$, and the optimising region

## 7.2 | Design variables

In this section, we describe the design variables we use to define the profile $\Gamma_{\mathcal{P}}$. To validate the proposed results and to explore new and more involved configurations, we consider two sets of design parameters. We refer to such design variables as `4pt` and `6pt` strategy. In the next paragraphs we describe both approaches in details.

*Four-point strategy,* `4pt`:
The magnetic pole $\Gamma_{\mathcal{P}}$ is parametrized by the position of four points

$$A(0, y_1),\ B(x_1, y_1),\ C(x_2, y_2) \quad \text{and} \quad D(x_3, y_2).$$

Such points depend on five variables, $x_1, x_2, x_3, y_1$, and $y_2$, see Figure 8. However, since the minimisation algorithm exploits semi-random walk to reach a local minimum, we have to impose some constraints on them [10]. First of all we have to impose that they are inside $\Omega_{\mathcal{O}}$. Then, since we know that the optimal does not present kinks, we impose

$$x_1 < x_2 < x_3,$$

and, since we know that it is dug, we require that

$$y_1 \geq y_2.$$

*Six-point strategy,* `6pt`:
In this case the magnetic pole $\Gamma_{\mathcal{P}}$ is parametrized by six points

$$A'(0, y_1),\ B'(x_1, y_2),\ C'(x_2, y_3),\ D'(x_3, y_4)$$

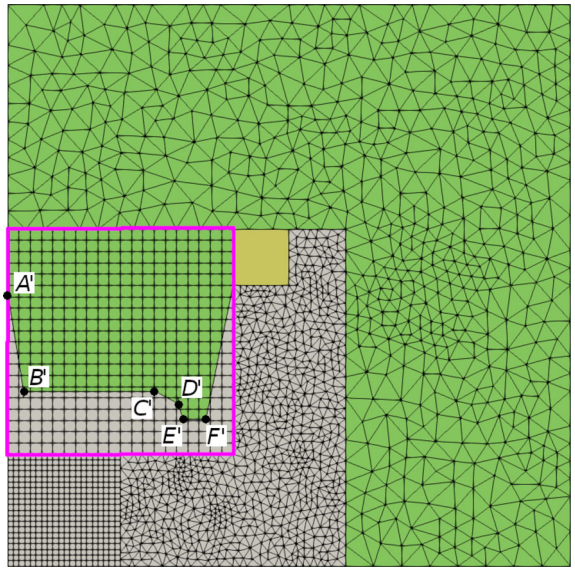


**FIGURE 9** Mesh of the computational domain where we take the `6pt` strategy. We also highlight the design points and the optimising region

$$E'(x_4, y_5), \quad \text{and} \quad F'(x_5, y_5).$$

Starting from this set of points, we are exploring more complex configuration, see Figure 9. Indeed, we have more points and parameters with respect to the previous case. Another important difference is that in the `4pt` strategy segments $\overline{AB}$ and $\overline{CD}$ are horizontal by construction, while in this case *only* the segment $\overline{E'F'}$ is forced to be horizontal.

As we have done before, we put some constraints on the values of such parameters. More specifically, we impose that they are inside $\Omega_{\mathcal{O}}$ and for the same reasons as before we force the conditions

$$x_1 < x_2 < x_3 < x_4 < x_5 \tag{21}$$

and

$$y_1 \geq y_2 \geq y_3 \geq y_4 \geq y_5 \,. \tag{22}$$

Consider one of the previous strategies to approximate of the magnet profile $\Gamma_{\mathcal{P}}$, then the optimal shape design problem can be formally cast as follows: Starting from an initial guess, find the design variables identifying the shape of the magnetic pole that gives the prescribed induction field $\mathbf{B}_0$ in the region of interests.

## 7.3 | Semi-random walk optimisation

To solve the optimisation process, we use the semi-random walk algorithm introduced in [10]. Starting from an initial guess, this procedure changes the value of the design variables to minimise a functional. In Figure 10 we show one run of such procedure considering the `4pt` strategy and the functional $\psi_1$.

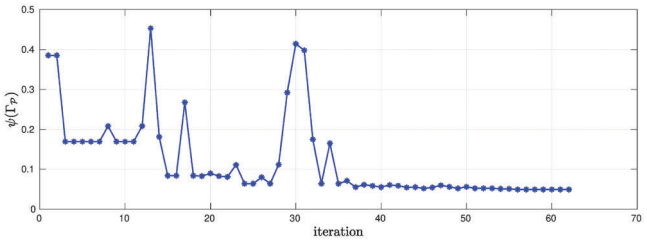


(a) History of $\psi_1(\Gamma_{\mathcal{P}})$.

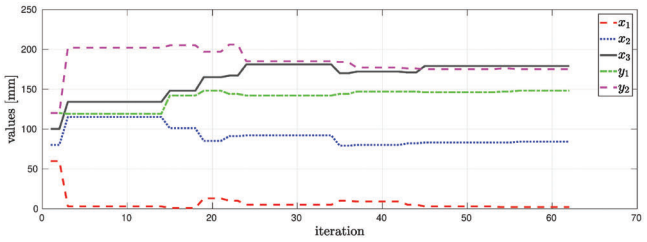


(b) The current best choice of design parameters.

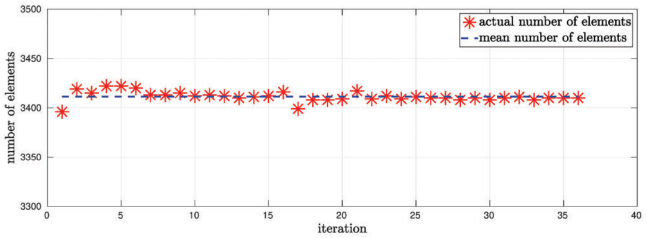


(c) The number of elements during optimisation.

**FIGURE 10** Analysis of one run of the proposed optimisation procedure

More specifically, in Figure 10a, we show the values of $\psi_1$ during the process. We observe that, since the proposed procedure uses a semi-random walk to enhance the exploration of the search-space, its trend is not monotonic.

In Figure 10b, we report the evolution of the actual best design variables. From those lines we can better realise that the optimising approach provides values that are far from the initial ones. Moreover, this plot is a numerical evidence of the fact that the proposed method does explore several configurations.

Finally, in Figure 10c, we show the number of mesh elements during the optimisation process. The VEM approach does not change so much the complexity of the mesh in terms of elements and, consequently, in terms of degrees of freedom. As a matter of fact we just 'draw' the profile $\Gamma_{\mathcal{P}}$ on a background mesh and cut elements so that the whole optimisation procedure is sped up.

In Figure 11 we give a more quantitative analysis about the results of the optimising process. We compare both components of the magnetic field $\mathbf{B}$ at the beginning, in black, and the end of the optimisation procedure, in red. From these data we see that the field becomes more uniform on the boundary and its magnitude is closer to the target value of 20 mT. Then, in Figure 12, we show the optimised profile. Such optimal configuration presents similar characteristics with respect to the ones already presented in the literature [10].

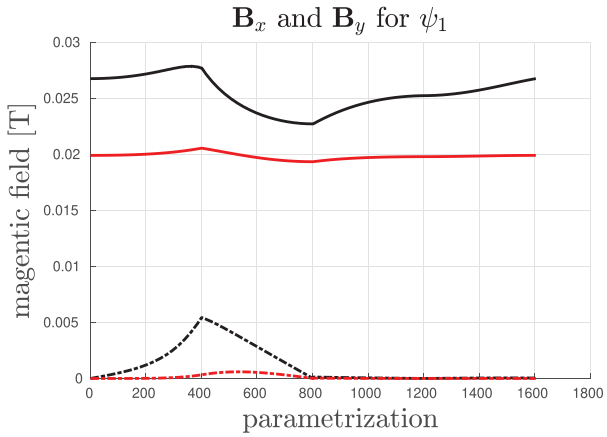


**FIGURE 11** Comparison between the initial and final values of **B**: in black the values associated with the initial configuration, in red the ones associated with the final one

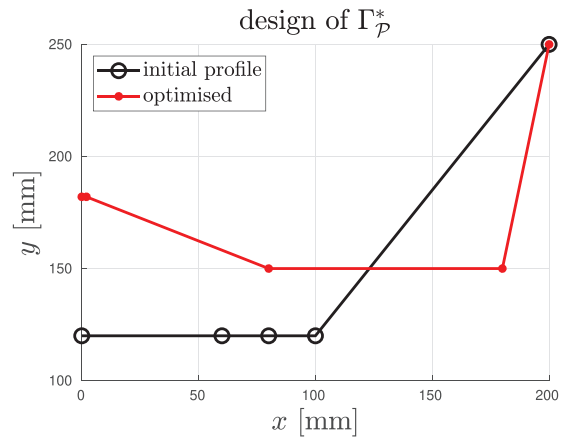


**FIGURE 12** Comparison between the initial and the optimised profile: in black the values associated with the initial configuration, in red the ones associated with the final one

## 7.4 | Numerical results

The optimisation problem at hand is challenging. Indeed, it is numerically ill-conditioned, that is, there exist many local minima very close to the global one characterised by different design variables.

From the analysis shown in Section 7.3, we understood that the proposed method is fast, effective, and based on a random walk. Consequently, in the numerical experiments described in this subsection, we do not focus on one specific run, but we collect many experiments starting from the same initial configuration to get different optimal configuration. We will summarise the result of all optimisation processed by showing the final design for each run where we lift such profiles according to the value of $\psi_1$: The more those profiles are close to the $xOy$ plane, the lower $\psi_1$ is. To facilitate such a comparison, we use a colour scale from dark to light red. More specifically, the initial configuration is black and the red colour associated

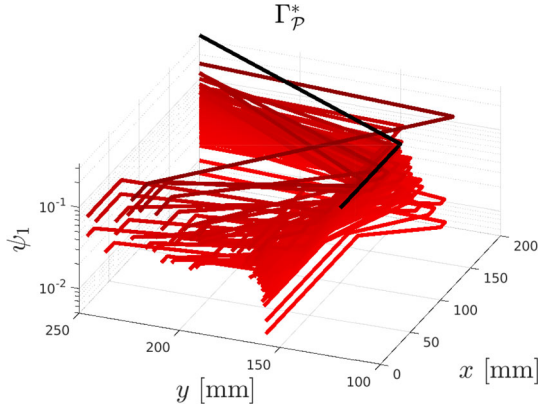


**FIGURE 13** Different results of `4pt` strategy with the functional $\psi_1$

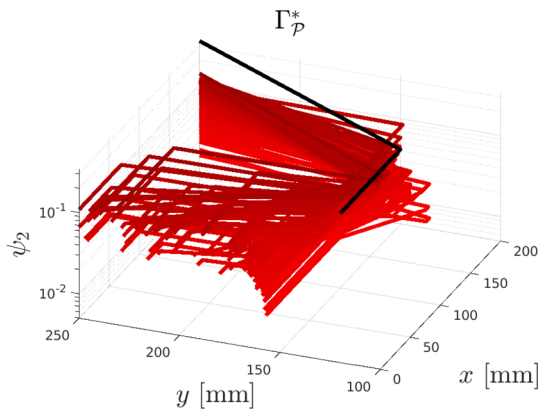


**FIGURE 14** Different results of `4pt` strategy with the functional $\psi_2$

with the final configuration is lighter if the value of $\psi_1$ is closer to zero.

### 7.4.1 | `4pt` strategy $\psi_1$ versus $\psi_2$

In this set of experiments we compare the results of the optimisation procedure driven by $\psi_1$ or $\psi_2$. For the last functional we take $\lambda = 0.25$ as a penalisation factor. To achieve this goal we run 100 of optimisation procedures driven by the functional $\psi_1$ and $\psi_2$, respectively. The results of all runs are shown in Figures 13 and 14. From such graphs we observe that the final optimised profiles are similar and in both cases we obtain a shape that is comparable to the ones found in the literature, see, for example, [10].

The functional we are trying to minimise presents many local minima but, thanks to the proposed semi-random walk procedure, we are able to explore several configurations. To give a further numerical evidence about this fact, we compute the variance of the design variables with respect to their initial values. In Table 1 we compute such a quantity only for the functional $\psi_1$, similar considerations can be done for $\psi_2$. All these variances, but $y_1$, have a value far from zero so the final optimal configuration is far from the initial one.

**TABLE 1** Variance of the design variables `4pt` strategy

| | $x_1$ | $x_2$ | $x_3$ | $y_1$ | $y_2$ |
|---|---|---|---|---|---|
| `run 1` | 0.9025 | 0.0689 | 0.3364 | 0.0584 | 0.5878 |
| `run 2` | 0.7511 | 0.1702 | 0.7225 | 0.0667 | 0.0951 |
| ⋮ | ⋮ | ⋮ | ⋮ | ⋮ | ⋮ |
| `run 20` | 0.0803 | 0.0756 | 0.2704 | 0.0506 | 1.0336 |
| ⋮ | ⋮ | ⋮ | ⋮ | ⋮ | ⋮ |
| `run 42` | 0.0278 | 0.8327 | 0.4356 | 0.0251 | 0.0951 |
| ⋮ | ⋮ | ⋮ | ⋮ | ⋮ | ⋮ |
| `run 61` | 0.0803 | 0.6006 | 0.2500 | 0.0117 | 0.1534 |
| ⋮ | ⋮ | ⋮ | ⋮ | ⋮ | ⋮ |
| `run 99` | 0.4225 | 0.7439 | 0.6561 | 0.0400 | 0.1167 |
| `run 100` | 0.5878 | 0.1139 | 0.8281 | 0.0625 | 0.1284 |
| `all` | 0.4374 | 0.4227 | 0.5951 | 0.0441 | 0.2570 |

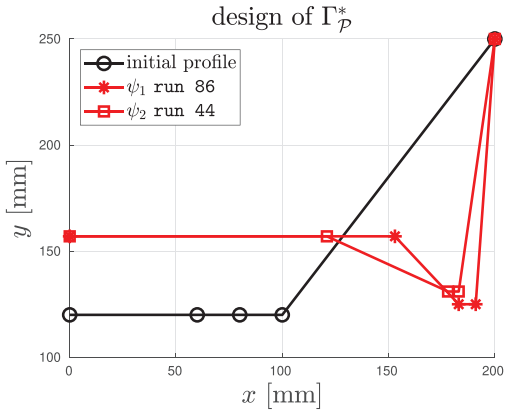


**FIGURE 15** Comparison between the final best profiles among all runs for both $\psi_1$ and $\psi_2$

Now we move on the analysis of the resulting magnetic fields and we verify that they are almost uniform inside $\Omega_I$ and close to the target value. To achieve this goal, in Figure 15 we show the initial and the final best profiles among all runs for both $\psi_1$ and $\psi_2$, which are `run 87` and `run 44`, respectively. The shape of both profiles is similar, the location of the recess is at the same position. Moreover, the values of the optimising variables $y_1$ coincide.

Recalling that in both figures we lifted the final configuration with the values of $\psi_1$, the optimisation process based on $\psi_2$ achieves approximately the same values of $\psi_1$, about $10^{-2}$. We analyse more in detail this aspect in Figures 16 and 17, where we show the absolute values of $\mathbf{B}_x$, dashed lines, and $\mathbf{B}_y$, full lines, along the boundary of the optimising region.

In both cases we see a great improvement, compare the black lines associated with the initial profile and the red ones that are associated with the optimal configuration found. However, the field associated with $\psi_1$ is closer to the uniform one: The red lines in Figure 16 are flatter with respect to the ones in Figure 17.

Moreover, other than getting an almost uniform field, its intensity is close to the target value, $\|\mathbf{B}_0\| = 20$ mT. Indeed, in

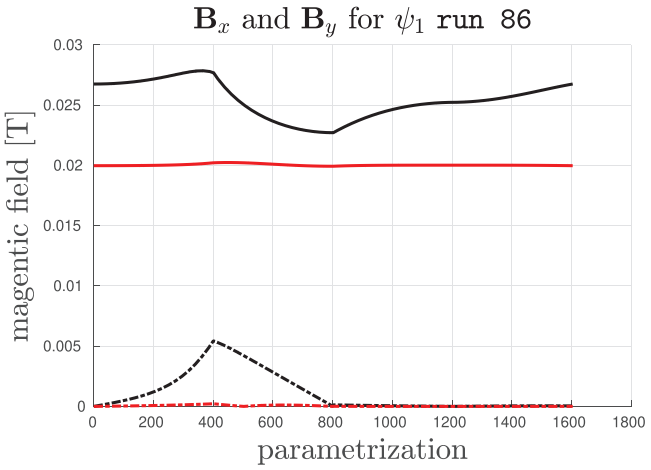


**FIGURE 16** Absolute values of $\mathbf{B}_x$, dashed lines, and $\mathbf{B}_y$, full lines, along the boundary of the optimising region for the best configuration made by `4pt` strategy with $\psi_1$

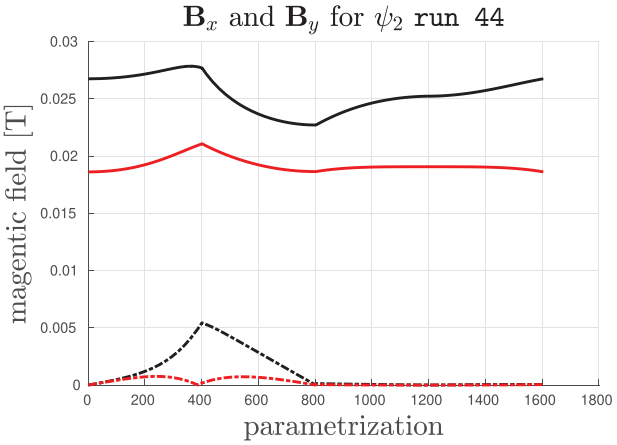


**FIGURE 17** Absolute values of $\mathbf{B}_x$, dashed lines, and $\mathbf{B}_y$, full lines, along the boundary of the optimising region for the best configuration made by `4pt` strategy with $\psi_2$

both cases $\mathbf{B}_x$, dashed red lines, are close to zero and $\mathbf{B}_y$, full red lines, are around 20 mT. Also in this case such a trend is better achieved via the optimisation guided by the functional $\psi_1$ with respect to the one guided by $\psi_2$.

### 7.4.2 | `4pt` strategy $\psi_1$ validity analysis

The idea of this experiment is to show the robustness of the proposed approach with respect to meshes. Indeed, we would like to verify that the final design is not affected by the refinement level of the region where we construct the magnet profile $\Gamma_{\mathcal{P}}$, $\Omega_{\mathcal{O}}$. To simplify the exposition, we consider only the optimisation strategy guided by $\psi_1$; similar considerations can be done for $\psi_2$.

We build three meshes where we consider three different level of refinement of $\Omega_{\mathcal{O}}$. We refer to such meshes as `level 1`, `level 2`, and `level 3`. In Figure 18 we show only the detail

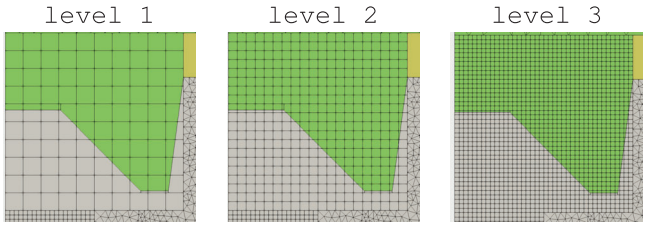


**FIGURE 18** Different refinement of the optimising region $\Omega_{\mathcal{O}}$

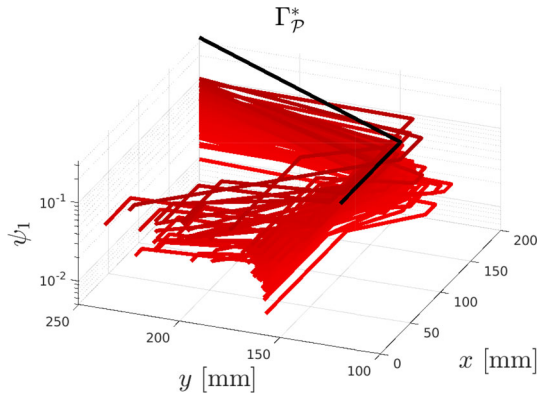


**FIGURE 19** Different results of `4pt` strategy with the functional $\psi_1$ and considering the `level 1` refinement of $\Omega_{\mathcal{O}}$

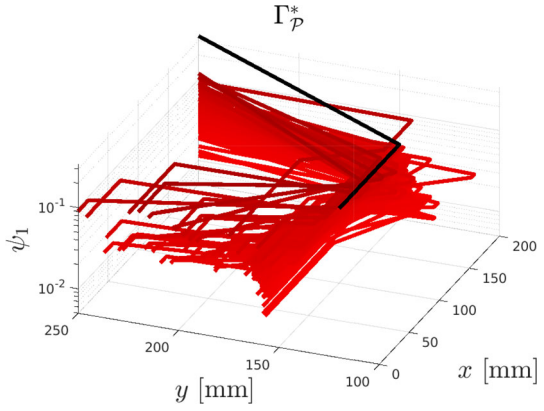


**FIGURE 20** Different results of `4pt` strategy with the functional $\psi_1$ and considering the `level 1` refinement of $\Omega_{\mathcal{O}}$

of such a region. Before showing the numerical experiments, we further underline that the flexibility of VEM in gluing meshes was the key point to generate such meshes. Indeed, one can extract $\Omega_{\mathcal{O}}$ from the domain $\Omega$, make the modifications *only* on this region, and then glue it back to $\Omega \backslash \Omega_{\mathcal{O}}$. The main advantage of such a procedure is that all the local mesh operations are made on a smaller mesh so the whole meshing procedure sped up.

The results associated with `level 2` are the ones discussed in the previous paragraph so they are summarised in Figure 13. For the remaining refinement levels we make 100 of runs as we did before. Such new results are reported in Figure 19 and Figure 20, for `level 1` and `level 3`, respectively.

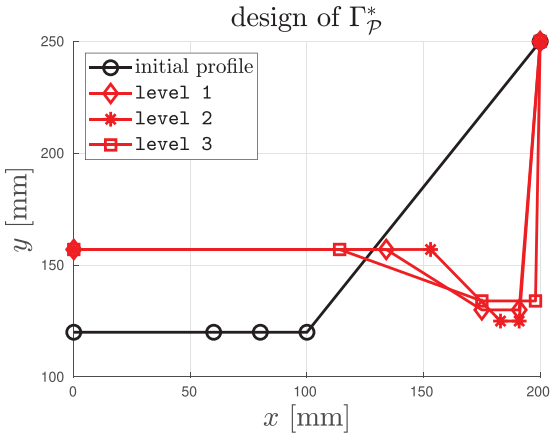


**FIGURE 21** Comparison among the best profiles resulted from the optimisation procedure with refinement `levels 1, 2,` and `3`

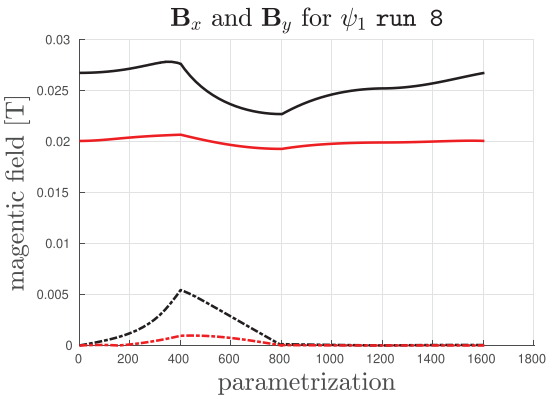


**FIGURE 22** Absolute values of $\mathbf{B}_x$, dashed lines, and $\mathbf{B}_y$, full lines, along the boundary of the optimising region for the best configuration made by `4pt` strategy with $\psi_1$ and `level 1` mesh

If we compare these three set of results, Figures 13, 19, and 20, we observe that they are similar each other and the final best configurations are associated with about the same value of $\psi_1$, that is, $10^{-2}$.

To prove this fact we compare the best profiles and the resulting magnetic field $\mathbf{B}$ along the boundary of the optimising region. In Figure 21 we show that the best designs are really close to each other. Indeed, all of them found the same optimal $y_1$ and the values of $y_2$ are close. Moreover, these three best profiles have the recess of $\Gamma_{\mathcal{P}}$ about at the same place.

In Figures 22 and 23 we show the values of $\mathbf{B}_x$ and $\mathbf{B}_y$ along the boundary of the optimising region for `level 1` and `3` meshes, the ones of `level 2` are shown in Figure 16. If we compare these three plots, we observe that the resulting magnetic fields are similar to each other and, as we observed in the previous example, they all fit the requirement of the target magnet field.

Such an experiment on the robustness of the optimising process with respect to the mesh is passed, that is, we can infer that the proposed method is not affected by the mesh

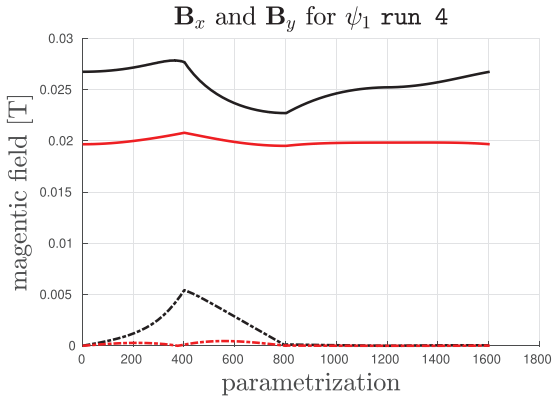


**FIGURE 23** Absolute values of $\mathbf{B}_x$, dashed lines, and $\mathbf{B}_y$, full lines, along the boundary of the optimising region for the best configuration made by `4pt` strategy with $\psi_1$ and `level 3` mesh

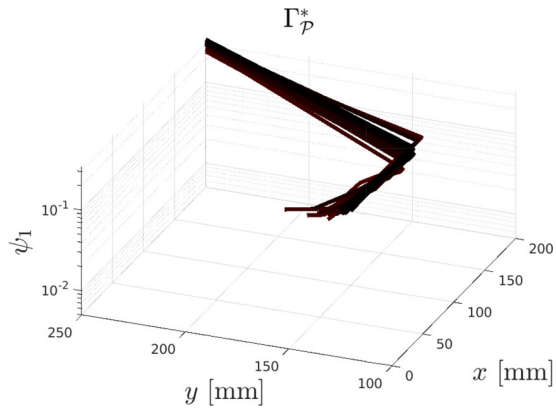


**FIGURE 24** Different results of `6pt` strategy with the functional $\psi_1$

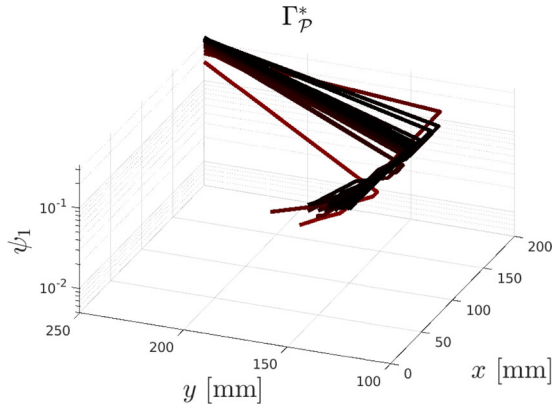


**FIGURE 25** Different results of `6pt` strategy with the functional $\psi_2$

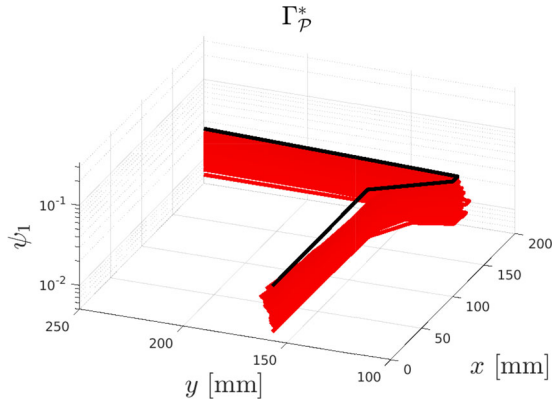


**FIGURE 26** Different results of `6pt` strategy with the functional $\psi_1$ starting from `run 86` of `4pt` strategy

in the optimising region $\Omega_{\mathcal{O}}$. Indeed, since we are considering a semi-random walk and a functional that is characterised by many local minima, we cannot claim to have exactly the same profiles but at least similar results.

### 7.4.3 | `4pt` versus `6pt` strategy

In this set of numerical examples we are considering the `6pt` strategy. We consider as initial profile the same of the previous experiments, see, for instance, the black line in Figure 15. Then, we run 100 of numerical optimisation processes for each functional $\psi_1$ and $\psi_2$.

In Figures 24 and 25 we collect all the final designs obtained by the optimisation procedure. If we compare such data with the corresponding ones using the `4pt` strategy, that is, compare Figure 13 with Figure 24 and Figure 14 with Figure 25, we notice that we do not reach the same good results as before. Indeed, the final optimal designs are associated with a not so low value of the target functional.

This fact is due to the semi-random walk procedure. Indeed, since we are considering 10 variables and the constraints defined in Equations (21) and (22), it is harder to find a set of numbers that satisfies such constraints. As a consequence the optimisation procedure does not explore so many configurations and it is not able to reduce much the objective functional.

### 7.4.4 | `6pt` strategy as new start

In the previous set of experiments we observe that the `6pt` strategy is not so effective if we consider as initial profile the same as the `4pt` strategy. To 'save' the `6pt` strategy, we decide to use the best result obtained by the `4pt` one as a trigger for it.

We consider only the optimisation procedure driven by the functional $\psi_1$ since this functional offers a more uniform distribution of the magnetic field $\mathbf{B}$ along the boundary of the optimising region.

In Figure 26 we show the final profiles of 100 runs starting from the best profile obtained via the `4pt` strategy, that is, `run 86`. From the data in such a figure we notice that the functional $\psi_1$ is further reduced, it is below $10^{-2}$.

Thanks to the new added points in the design of the profile, the shape of the magnet profile is 'refined', see Figure 27. The new added point $E'$ smooths the profile of the magnet on the right part, while the point $B'$ does not affect the shape of

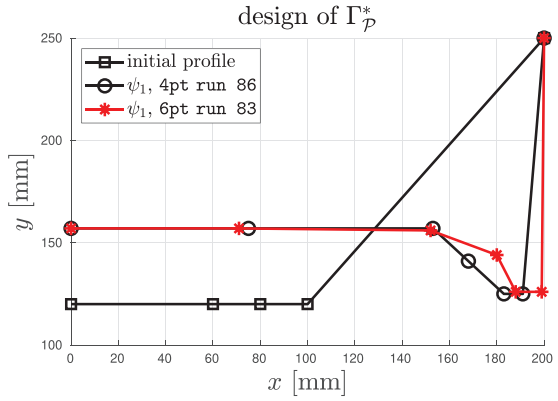


**FIGURE 27** Comparison between the initial final best profile among all runs for $\psi_1$ using `6pt` strategy and the best result of the `4pt` strategy

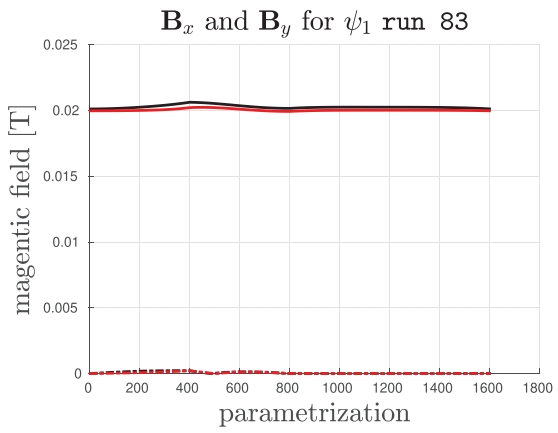


**FIGURE 28** Absolute values of $\mathbf{B}_x$, dashed lines, and $\mathbf{B}_y$, full lines, along the boundary of the optimising region for the best configuration made by `6pt` strategy with $\psi_1$

the optimal profile. Indeed, we still have a flat profile on the left part.

This further improvement on the shape of magnet profile becomes more evident from Figure 28. Here, we compare the values of the magnetic field associated with the functional $\psi_1$ via `4pt` strategy, the black lines, and the values of `run 83` of `6pt` strategy triggered by `run 86` of `4pt` strategy, in red. The good result of the first optimisation strategy is further improved by this new run. Indeed, the field is more uniform and closer to the target value.

## 8 | CONCLUSION

The paper summarises the theoretical aspects behind the VEM based on potential formulation and presents an original technique of meshing for two-dimensional domains. In particular, the flexibility of VEM in mesh generation for complex computational domains is described and it is shown that such flexibility can be further exploited combining virtual and FE approaches. This way, one can use local spaces over elements characterised by hanging nodes and polygonal geometries combined with standard FEs over triangles and squares.

This approach puts the ground for an original technique for handling the shape variation in a problem of optimal shape design. The promising results encourage further investigations in this field.

## CONFLICT OF INTEREST

The authors have declared no conflict of interest.

## DATA AVAILABILITY STATEMENT

Data available on request from the authors.

## ORCID

*F. Dassi* https://orcid.org/0000-0001-5590-3651

## REFERENCES

1. Beirão da Veiga, L., Brezzi, F., Cangiani, A., Manzini, G., Marini, L.D., Russo, A.: Basic principles of virtual element methods. Math. Models Methods Appl. Sci. 23(1), 199–214 (2013)
2. Dassi, F., Di Barba, P., Russo, A.: Virtual element method and permanent magnet simulations: potential and mixed formulations. IET Sci. Meas. Technol. 14(10), 1098–1104 (2020)
3. Dassi, F., Di Barba, P., Russo, A.: The virtual element method for magnetostatics: two possible approaches. International Compumag Society Newsletter, Invited Contribution 28(1), 3–14 (2021)
4. Di Pietro, D.A., Droniou, J.: An arbitrary-order method for magnetostatics on polyhedral meshes based on a discrete de rham sequence. J. Comput. Phys. 429, 109991 (2021)
5. Chave, F., Di Pietro, D.A., Lemaire, S.: A discrete Weber inequality on three-dimensional hybrid spaces with application to the HHO approximation of magnetostatics. Math. Models Methods Appl. Sci. 32(1), 175–207 (2022)
6. Chen, G., Cui, J., Xu, L.: Analysis of a hybridizable discontinuous Galerkin method for the Maxwell operator. ESAIM: Math. Model. Numer. Anal. 53(1), 301–324 (2019)
7. Chen, H., Qiu, W., Shi, K., Solano, M.: A superconvergent HDG method for the Maxwell equations. J. Sci. Comput. 70(3), 1010–1029 (2016)
8. Perugia, I., Schötzau, D., Monk, P.: Stabilized interior penalty methods for the time-harmonic Maxwell equations. Comput. Methods Appl. Mech. Eng. 191(41), 4675–4697 (2002)
9. Pironneau, O.: Optimal shape design for elliptic systems. In: System Modeling and Optimization, pp. 42–66. Springer, Berlin Heidelberg (1982)
10. Wiak, S., Di Barba, P., Dughiero, F., Sieni, E.: Non-parametric optimal shape design of a magnetic device for biomedical applications. COMPEL – Int. J. Comput. Math. Electr. Electron. Eng. 31(5), 1358–1367 (2012)
11. Sohn, D., Han, J., Cho, Y., Im, S.: A finite element scheme with the aid of a new carving technique combined with smoothed integration. Comput. Methods Appl. Mech. Eng. 254, 42–60 (2013)
12. Armstrong, A.G., Fan, M., Simkin, J., Trowbridge, C.: Automated optimization of magnet design using the boundary integral method. IEEE Trans. Magn. 18(2), 620–623 (1982)
13. Di Barba, P., Evelina Mognaschi, M., Lowther, D.A., Sykulski, J.K.: A benchmark team problem for multi-objective Pareto optimization of electromagnetic devices. IEEE Trans. Magn. 54(3), 1–4 (2017)
14. Di Barba, P., Dughiero, F., Sieni, E.: Magnetic field synthesis in the design of inductors for magnetic fluid hyperthermia. IEEE Trans. Magn. 46(8), 2931–2934 (2010)
15. Di Barba, P., Dughiero, F., Sieni, E., Candeo, A.: Coupled field synthesis in magnetic fluid hyperthermia. IEEE Trans. Magn. 47(5), 914–917 (2010)
16. Henrot, A., Pierre, M.: Shape Variation and Optimization. European Mathematical Society Publishing House (2018)
17. Goya, G.F., Grazu, V., Ricardo Ibarra, M.: Magnetic nanoparticles for cancer therapy. Curr. Nanosci. 4(1), 1–16 (2008)

18. Hildebrandt, B., Wust, P., Ahlers, O., Dieing, A., Sreenivasa, G., Kerner, T., Felix, R., Riess, H.: The cellular and molecular basis of hyperthermia. Crit. Rev. Oncol. Hematol. 43(1), 33–56 (2002)
19. Krishnan, K.M.: Biomedical nanomagnetics: a spin through possibilities in imaging, diagnostics, and therapy. IEEE Trans. Magn. 46(7), 2523–2558 (2010)
20. Candeo, A., Dughiero, F.: Numerical FEM models for the planning of magnetic induction hyperthermia treatments with nanoparticles. IEEE Trans. Magn. 45(3), 1658–1661 (2009)
21. Gneveckow, U., Jordan, A., Scholz, R., Brüß, V., Waldöfner, N., Ricke, J., Feussner, A., Hildebrandt, B., Rau, B., Wust, P.: Description and characterization of the novel hyperthermia-and thermoablation-system for clinical magnetic fluid hyperthermia. Med. Phys. 31(6), 1444–1451 (2004)
22. Rosensweig, R.E.: Heating magnetic fluid with alternating magnetic field. J. Magn. Magn. Mater. 252, 370–374 (2002)
23. Bianchi, N.: Electrical Machine Analysis Using Finite Elements. CRC Press, Boca Raton, FL (2017)
24. Beirão da Veiga, L., Brezzi, F., Marini, L.D., Russo, A.: Virtual element methods for general second order elliptic problems on polygonal meshes. Math. Models Methods Appl. Sci. 26, 729–750 (2016)
25. Beirão da Veiga, L., Brezzi, F., Dassi, F., Marini, L.D., Russo, A.: Virtual element approximation of 2d magnetostatic problems. Comput. Methods Appl. Mech. Eng. 327, 173–195 (2017). [Advances in Computational Mechanics and Scientific Computation–The Cutting Edge.]
26. Beirão da Veiga, L., Brezzi, F., Marini, L.D., Russo, A.: The hitchhiker's guide to the virtual element method. Math. Models Methods Appl. Sci. 24(08), 1541–1573 (2014)
27. Marechal, Y.: Some meshless methods for electromagnetic field computations. IEEE Trans. Magn. 34(5), 3351–3354 (1998)
28. Ho, S.L., Yang, S., Machado, J.M., Wong, H.C.: Application of a meshless method in electromagnetics. IEEE Trans. Magn. 37(5), 3198–3202 (2001)
29. Li, Q., Lee, K.: An adaptive meshless method for magnetic field computation. IEEE Trans. Magn. 42(8), 1996–2003 (2006)
30. Buffa, A., Maday, Y., Rapetti, F.: A slideing mesh-mortar method for a two dimensional currents model of electric engines. ESAIM: Math. Model. Numer. Anal. 35(2), 191–228 (2001)
31. Bernardi, C., Maday, Y., Patera, A. T.: A new nonconforming approach to domain decomposition: the mortar element method. In: Nonlinear Partial Differential Equations and Their Applications, pp. 13–51. Harlow: Longman Scientific & Technical, New York: John Wiley & Sons, Inc (1994)

**How to cite this article:** Dassi F., Di Barba P., Russo A.: A free-cutting mesh strategy for optimal shape synthesis in magnetics. IET Sci. Meas. Technol. 16, 337–352 (2022). https://doi.org/10.1049/smt2.12108